Physics of Fluids

RESEARCH ARTICLE | OCTOBER 27 2022

Feasibility of hydrodynamically activated valves for salp-like propulsion

Xiaobo Bi (毕晓波) ; Hui Tang (唐辉) ; Qiang Zhu (朱强)

Physics of Fluids 34, 101903 (2022)
https://doi.org/10.1063/5.0126809

Physics of Fluids ARTICLE scitation.org/journal/phf

Feasibility of hydrodynamically activated valves for salp-like propulsion

Cite as: Phys. Fluids 34, 101903 (2022); doi: 10.1063/5.0126809
Submitted: 17 September 2022 · Accepted: 5 October 2022 ·
Published Online: 27 October 2022

View Online Export Citation CrossMark

Xiaobo Bi (毕晓波),[1] Hui Tang (唐辉),[1] and Qiang Zhu (朱强)[2,a]

AFFILIATIONS

[1]Department of Mechanical Engineering, The Hong Kong Polytechnic University, Hung Hom, Kowloon, Hong Kong 999077, People's Republic of China
[2]Department of Structural Engineering, University of California San Diego, La Jolla, California 92093-0085, USA

[a]Author to whom correspondence should be addressed: qizhu@ucsd.edu

ABSTRACT

Using valves to control the direction of internal flow for effective swimming, the jet-propulsion method of sea salp (a barrel-shaped marine invertebrate) provides a promising locomotion mechanism for bio-inspired robots. In this study, we numerically investigate this problem via an axisymmetric fluid–structure interaction model within the immersed-boundary framework. Specifically, we prove that in these systems, it is feasible to use fully passive valves whose opening and closing actions are driven solely by the hydrodynamic load. This finding is going to greatly reduce the complexity of locomotion devices based on this design. Furthermore, we have examined the effect of the design parameters, i.e., the stiffness and inertia, of the valves upon the swimming performance. In general, it is found that stiff and heavy valves increase the swimming speed, whereas soft and light valves decrease the cost of transport.

I. INTRODUCTION

With impressive speed and maneuverability, the jet-propulsion capacity of soft-body aquatic creatures, such as squid, has inspired the development of novel underwater robots with deformable bodies.[1–4] In its jetting mode, squid locomotion involves intermittent bursts driven by cyclic expansion and shrinking of it body. To elaborate, a squid first inflates its mantle cavity to suck water in through a mantle aperture. Afterward, the body shrinks and water is discharged out rapidly through a narrow funnel tube on the same side of the body as the mantle aperture. During this process, ultra-fast motion can be achieved. For example, small squid (e.g., the larvae of *Loligo vulgaris*) can reach a bursting speed of 25 body lengths per second (BL/s).[5] Larger ones (e.g., *Loligo opalescens*) can also reach a maximum speed of 10 BL/s.[6] Moreover, squid are capable of pointing the funnel tube in any direction for maneuvering via thrust vectoring. For these reasons, squid locomotion has recently been studied extensively to explore the underlying physical mechanisms and design principles.[7] The primary efforts were on the understanding of fluid–structure interactions associated with the body deformation,[8–12] the impact of added-mass related force,[13,14] the vortex ring dynamics,[15–17] and the effect of the nozzle configuration.[18]

Among these mechanisms, the procedure of energy exchange during the refilling–discharging cycle is particularly important since it is directly related to the efficiency of locomotion. For instance, in our recent study, the effect of the fluid field inside the internal cavity (hereafter referred to as the pressure chamber) upon the energetics has been examined.[19] The results show that the kinetic energy of the refilling flow is mainly dissipated away in the pressure chamber rather than contributing to the subsequent jetting, which compromises the efficiency of the system. This is because the mantle aperture and funnel tube of a squid are both located in the head side so that the refilling flow and the jet flow are in opposite directions. In squid swimming, this issue is partially solved by reducing the speed, and subsequently the kinetic energy, of the refilling flow using an inlet (the mantle aperture) much larger in the cross-sectional area than the outlet (the funnel tube).

Sea salps, on the other hand, use a different method for performance enhancement by positioning the flow inlet and outlet at opposite ends of the body.[20,21] The jet-propulsion method of salps bears certain resemblance to that of squid because they both utilize refilling-jetting cycles to inhale and expel fluid through body deformation. The difference lies in the detailed configuration. Unlike squid, a salp's water entrance (the *oral syphon*) is located on the front side, while the exit (the *atrial syphon*) is located on the rear side. During the refilling phase, the atrial syphon is closed and the oral syphon is open to let water in. During the jetting phase, the oral syphon is closed and the atrial syphon is open to let water out. This unique arrangement enables a uni-directional flow inside the chamber during an entire refilling-jetting cycle, which might reduce energy waste and enhance the propulsive efficiency.[22]

Despite its potential applications in bio-inspired engineering, salp-like swimming has been mostly neglected in the literature. A notable study was conducted by Sutherland and Madin,[23] who experimentally observed the wake near solitary salps via Particle Image Velocimetry (PIV) and identified two distinct vorticity patterns. The first pattern is characterized by a single vortex ring, and the second one features a combination of a leading vortex ring followed by a trailing vorticity distribution. These patterns are consistent with the behavior of vortices formed by pulsed jets, in which a dimensionless parameter called the *formation number* plays an important role.[24] Other studies on this topic include a theoretical analysis that investigates the aggregated salp locomotion,[25] a numerical work that explores the impact of jet angle on the swimming performance or aggregated salps,[26] and investigations of synthetic jets that share some physical characteristics with the propulsion mechanism of salps.[27] However, none of these studies considers the unsteady fluid–structure coupling involved in the salp inflation–deflation cycles.

Recently, we developed an axisymmetric numerical model within the immersed boundary framework to investigate the fluid dynamics of a salp-like self-propelled system.[22] The system consists of three components, a deformable shell, and two valves on the front and rear sides. The body deformation and the valve motions are prescribed. Through coordinated valve opening–closing motions and body inflation–deflation cycles, pulsed jetting and subsequent forward motion are achieved. In this scenario, the refilling flow originated from the front valve during the inflation phase goes directly to the rear valve to join the jet. This uni-directional internal flow successfully mitigates the energy dissipation that occurs in the pressure chamber and improves the swimming efficiency. Moreover, the study shows that there exists an energy recovery mechanism in the salp-like swimming system: the energy expended by one component can be partially recovered by other components through hydrodynamic interactions. This phenomenon suggests that the system can be improved by replacing the actively controlled valves with passive ones. Without extra energy input, the passive valves can be activated by hydrodynamically harvesting energy spent by the shell.

Indeed, to actively control the opening and closing motions of valves complicated controlling and actuation systems are necessary. In addition, non-optimized valve motions may create large drag force and slow down the system when the valves move against the flow. This issue may be avoided through self-adaptive motions of passive valves since they usually move in the direction of the local flow.

In the present study, we investigate the feasibility and reliability of passive valves in a salp-like swimmer. Toward this end, we develop an axisymmetric numerical model in which the rotations of the valves are activated by hydrodynamic load. Through simulations, we examine the locomotion performance of such a system and explore effects of the structural properties (e.g., rotational inertia and stiffness) of the valves.

The rest of this paper is organized in the following manner. We begin by defining the configuration and kinematics of the salp-like system, followed by a brief description of the mathematical formulation and numerical algorithm. After that, simulation results and discussions are presented. Finally, conclusions will be drawn.

II. PHYSICAL DESCRIPTION

As displayed in Fig. 1, the model that we consider is an axisymmetric propulsion system, which contains a deformable shell and two rigid one-way valves. The contour of the shell is a semi-ellipse whose semi-axis is a and major axis is L. The major axis is $D/2$ above the axis of symmetry. In three dimensions, the shell forms a body of revolution with two orifices whose diameters are D in the front and rear ends. Designed to control the opening and closing actions of the orifices, the two valves with contour length of $D/2$ are connected to the shell edges with torsional springs $k_{\theta f}$ and $k_{\theta b}$. Hereafter, we use subscripts "f" and "b" to represent quantities related to the front valve and the back valve, respectively. The springs are in natural states when the valves are closed, i.e., $\theta_f = \theta_b = 0$.

Physically, the valve model that we use may represent a valve made of azimuthally distributed ribs connected by an elastic membrane. With a length of $D/2$, each rib is rigid and allowed to rotate around a hinge, where a torsional spring is installed. The surface area of the elastic membrane varies when the valve opens or closes. Even though there exist other designs of one-way valves that do not resemble our model, these designs all share the primary characteristics of our model, inertia, and stiffness. Therefore, our analysis can be qualitatively applied to a wide range of valve designs.

The refilling-jetting cycle of the system is achieved by cyclic inflation–deflation deformations of the shell, which is accomplished through varying the semi-minor axis a with the major axis L being fixed. Within a deformation period T, we prescribe a as

$$a(t) = a_0 + (a_1 - a_0)[1 - \cos(2\pi t/T)]/2, \tag{1}$$

in which a_0 and a_1 correspond to fully deflated and fully inflated states, respectively. These two parameters determine the stroke ratio, defined as $4\Delta\forall/(\pi D^3)$, where $\Delta\forall$ is the discharged volume during a single jetting. This dimensionless parameter governs the vortex pattern in the wake and plays an important role in thrust generation.[9,16,24]

The rotations of the valves are restricted within the range of $[0, \pi/2]$, in which the rotations of the two valves are determined by the conservation of angular momentum, i.e.,

$$I_{\theta f}\ddot{\theta}_f + k_{\theta f}\theta_f = M_f \quad \text{and} \quad I_{\theta b}\ddot{\theta}_b + k_{\theta b}\theta_b = M_b, \tag{2}$$

where $I_{\theta f}$ and $I_{\theta b}$ represent the moments of inertia of the two valves. M_f and M_b are the hydrodynamic moments exerted on them.

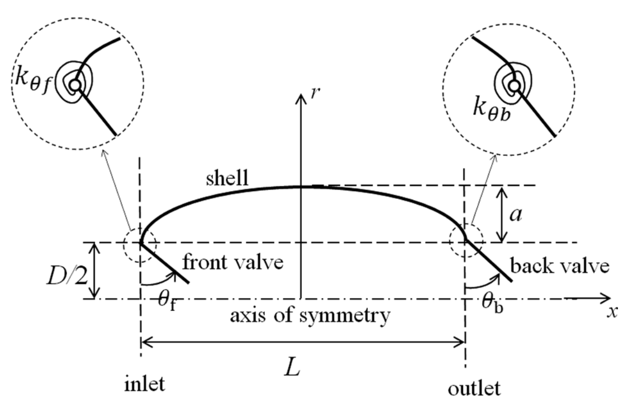

FIG. 1. Schematic illustration of the salp-like swimming system.

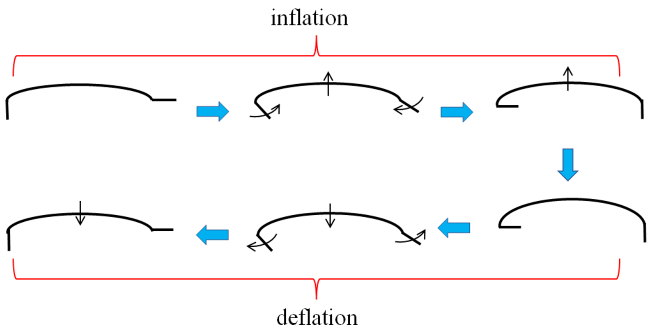

FIG. 2. The deformation of the shell and opening/closing motions of the valves during one inflation-deflation cycle.

As shown in Fig. 2, the initial shape of the shell is in the fully deflated slender state (i.e., $a = a_0$) and the front valve is initially closed (i.e., $\theta_f = 0$), while the back valve is completely open (i.e., $\theta_b = \pi/2$). During the inflation phase ($0 \le t \le T/2$), the semi-minor axis is increased to a_1, which is accompanied by the closing process of the back valve driven by the back spring $k_{\theta b}$ and the low pressure inside the chamber, and the opening of the front valve driven by the refilling flow. Therefore, fluid is mostly absorbed from the front orifice. At the end of the inflation phase, the front (or back) valve may not be completely open (or closed) due to the passive dynamics. During the deflation phase ($T/2 \le t \le T$), the semi-minor axis goes back to a_0 to expel fluid out of the chamber. This is accompanied by the closing of the front valve driven by the front spring $k_{\theta f}$ and the high pressure inside the chamber and the opening of the back valve driven by the outgoing flow. As a result, the fluid is mostly discharged through the back orifice, forming a jet flow in the wake and generating thrust.

III. MATHEMATICAL FORMULATION AND NUMERICAL ALGORITHM

The governing equations and numerical algorithm including the fluid–structure coupling method have been well documented in our previous publications,[9,28] in which the accuracy and robustness of the numerical solver were also validated through simulations of benchmark problems. We only briefly introduce the key features of the numerical model.

Defined in a cylindrical coordinate $\mathbf{x} \equiv (x, r)$, where x is the longitudinal direction and r the radial direction, the hydrodynamic problem is governed by an axisymmetric representation of the incompressible Navier–Stokes equations expressed as

$$\begin{aligned}
&\rho\left(\frac{\partial u_x}{\partial t} + u_x\frac{\partial u_x}{\partial x} + u_r\frac{\partial u_x}{\partial r}\right) \\
&\quad = -\frac{\partial p}{\partial x} + \mu\left(\frac{\partial^2 u_x}{\partial x^2} + \frac{\partial^2 u_x}{\partial r^2} + \frac{\partial u_x}{r\partial r}\right) + f_x, \\
&\rho\left(\frac{\partial u_r}{\partial t} + u_x\frac{\partial u_r}{\partial x} + u_r\frac{\partial u_r}{\partial r}\right) \\
&\quad = -\frac{\partial p}{\partial r} + \mu\left(\frac{\partial^2 u_r}{\partial x^2} + \frac{1}{r}\frac{\partial}{\partial r}\left(\frac{r\partial u_r}{\partial r}\right) - \frac{u_r}{r^2}\right) + f_r, \\
&\frac{\partial u_x}{\partial x} + \frac{1}{r}\frac{\partial (r u_r)}{\partial r} = 0,
\end{aligned} \tag{3}$$

where $\mathbf{u} \equiv (u_x, u_r)$ is the fluid velocity, p is the pressure, ρ is the fluid density, and μ is the fluid viscosity. $\mathbf{f} \equiv (f_x, f_r)$ is the fluid–structure interacting force density, obtained through the following rendition using the two-dimensional Dirac delta function:

$$\mathbf{U}(s,t) = \int_\Omega \mathbf{u}(\mathbf{x},t)\delta(\mathbf{x} - \mathbf{X}(s,t))d\mathbf{x}, \tag{4}$$

$$\partial \mathbf{X}(s,t)/\partial t = \mathbf{V}(s,t), \tag{5}$$

$$\mathbf{F}(s,t) = \alpha\int_0^t [\mathbf{U}(s,\tau) - \mathbf{V}(s,\tau)]d\tau + \beta[\mathbf{U}(s,t) - \mathbf{V}(s,t)], \tag{6}$$

$$\mathbf{f}(\mathbf{x},t) = \int_\Gamma \mathbf{F}(s,t)\delta(\mathbf{X}(s,t) - \mathbf{x})ds, \tag{7}$$

where s stands for a Lagrangian coordinate along the structural body $\Gamma = \Gamma_f + \Gamma_s + \Gamma_b$. Γ_f, Γ_s, and Γ_b represent the front valve, the body shell, and the back valve, respectively. $\boldsymbol{\Omega}$ is the fluid domain. $\mathbf{X}$ and $\mathbf{V}$ are the structural particle location and velocity, respectively. The parameters α and β are sufficiently large negative numbers, which are applied to enforce the consistency in terms of velocities and positions between the neighboring fluid and structure elements so that the no-flux and no-slip conditions at the fluid–structure interface are satisfied. The specific values of these two parameters do not affect the simulation results because the obtained penalty force $\mathbf{F} \equiv (F_x, F_r)$ will eventually converge to the desired fluid–structure interaction force after iterations.

The Navier–Stokes equations are discretized temporally with the Crank–Nicholson scheme and spatially with a second-order finite difference algorithm in Eulerian staggered grids. The implicit treatment of the convective term makes the equations nonlinear. We linearize the system with a second-order temporal factorization method.[29] Lower–Upper (LU) decomposition is then employed to decouple the flow velocity and pressure to avoid inversion of large sparse matrices. During one time step, a provisional velocity field is first obtained based on the flow field information at the previous time step. It is then used to update the pressure field. Afterward, the flow velocity field is updated with the new pressure field to fulfill mass conservation.[8,30]

The translational motion of the body in the horizontal direction is governed by Newton's equation,

$$m_c \ddot{x}_c = F_n, \tag{8}$$

where m_c is the mass of the body, x_c is the location of the center of mass, whose positive direction is $-x$ (for simplicity, the front and back valves are not considered when we determine the center of mass), and F_n is the net horizontal force on the body, obtained as

$$F_n = -\int_\Gamma 2\pi r(s)F_x(s,t)ds. \tag{9}$$

The angular motions of the two valves are governed by Eq. (2), in which the fluid-induced moments acting on the valves are calculated by

$$M_f = -\int_{\Gamma_f} 2\pi r(s)\mathbf{F}(s)\cdot\mathbf{r}(s)ds, \quad M_b = -\int_{\Gamma_b} 2\pi r(s)\mathbf{F}(s)\cdot\mathbf{r}(s)ds, \tag{10}$$

where $\mathbf{r}(s)$ is the arm of the force $\mathbf{F}(s)$ with respect to the spin axis.

Unlike the deformation of the shell that is prescribed with Eq. (1), both the forward motion of the body and the rotations of the valves are coupled with the fluid dynamics. The interactions of the fluid solver and Eqs. (2) and (8) are accomplished through a feedback scheme.[8,28,30]

IV. RESULTS

By using the algorithm described in Sec. III, we numerically examine the dynamics of the system shown in Fig. 1. The purposes of our simulations are (1) to determine the feasibility of passively activated valves in this system and (2) to evaluate the effects of the parameters of the valves, i.e., the stiffness and inertia, upon the performance of the system.

Toward this end, we study two scenarios, tethered and free swimming. In the tethered mode, the center of mass of the body is kept unmoving so that $u_c \equiv \dot{x}_c = 0$. In the free-swimming mode, the system is allowed to move forward according to Newton's law [Eq. (8)].

Without the disturbance in the flow field and hydrodynamic load caused by forward motion, in the tethered setup, the one-way valves are the only factor that breaks the forward-aft symmetry of the system so that non-zero thrust can be created. This scenario provides a clean setup to test the dynamics of the valves and their role in thrust generation. The free-swimming scenario, on the other hand, demonstrates the actual performance of the system.

We nondimensionalize the problem by choosing the body length L, the fluid density ρ, and the deformation cycle T as repeating variables. In practice, this is conveniently achieved by setting the values of these three parameters to be unity. The normalized values of some parameters are fixed in the following simulations, including the dynamic viscosity of the fluid ($\mu = 0.005$), the mass of the body ($m_c = 0.05$), the diameter of the inlet and outlet ($D = 0.15$), and the lengths of the semi-minor axis of the shell in its deflated and inflated states ($a_0 = 0.05$, $a_1 = 0.07$). Correspondingly, the jet-related Reynolds number R_{ej}, defined as $\rho D\tilde{u}/\mu$, where $\tilde{u}$ is the peak value of the spatially averaged outflow speed at the outlet obtained as $(d\forall/dt)/(\pi D^2/4)|_{max}$, is around 67. The stroke ratio is 4.7. This particular stroke ratio is close to the formation number, a stroke ratio corresponding to the formation of a single strongest vortex ring after each discharge.[24] It is believed to be the case with optimal energy efficiency in pulsed-jet propulsion since the vortex ring generated this way contains maximum impulse for given energy spent.[7,31,32] For simplicity, we assume that the front and back valves share the same properties, i.e., $I_{\theta f} = I_{\theta b} = I_\theta$ and $k_{\theta f} = k_{\theta b} = k_\theta$.

The numerical parameters are chosen based on sensitivity tests conducted in previous studies.[9,18] The size of the computational domain is chosen to be 5×1. The finest fluidic grid near the body is $\Delta x = \Delta r = 0.003$. Along the body (including the shell and the two valves), 300 uniformly distributed grids are used. The time step is $\Delta t = 10^{-4}$.

In all the following simulations, the one-cycle responses are obtained in the ninth cycle, when the steady-state (cyclic) responses have already been established. For convenience, in these plots, the starting time of the cycle is shifted from $t = 8$ to $t = 0$. The time-averaged values are also obtained within this cycle. These quantities are distinguished with an overline.

A. Tethered mode

We start by considering the tethered mode in which the body has no forward motion so that the swimming speed $u_c = 0$. The performance of the system in this mode is characterized by two quantities, the time-averaged net force generation $\bar{F}_n$, and the time-averaged power expenditure $\bar{P}_s$, where P_s is the instantaneous power expenditure at the shell defined as $P_s = \int_{\Gamma_s} 2\pi r \mathbf{F} \cdot \mathbf{U} ds$. The power expenditures on the front and back valves are $P_f = \int_{\Gamma_f} 2\pi r \mathbf{F} \cdot \mathbf{U} ds$ and $P_b = \int_{\Gamma_b} 2\pi r \mathbf{F} \cdot \mathbf{U} ds$, respectively.

In the first case, the stiffness and inertia of the valves are chosen as $k_\theta = 10^{-4}$ and $I_\theta = 10^{-4}$. In Fig. 3(a), we plot the variations of the valve positions, represented by rotational angles θ_f and θ_b, within a refilling–discharging cycle in the steady state. The valves are closed when their corresponding rotational angles are zero, and fully opened when these angles are $\pi/2$. In the figure, it is seen that at the beginning of the inflation phase ($0 \le t \le 1/2$), θ_f increases from 0 to $\pi/2$, while θ_b decreases to 0, corresponding to the opening of the front valve and the closing of the back valve. When deflation starts ($t > 1/2$), θ_f drops back to 0 while θ_b rises to $\pi/2$, so that the front valve is closed and the back valve is opened. This is exactly the targeted opening/closing motions of the two valves described in Fig. 2.

Figure 3(b) demonstrates the power expenditures at the shell (P_s) and the two valves (P_f and P_b). It is seen that most power expenditure at the shell P_s occurs near the early stages of the inflation and deflation phases, since at those stages, mechanical energy is needed not only to move the fluid but also to push the valves. P_f and P_b are mostly negative during both inflation and deflation, indicating that they absorb energy from the flow field in both processes. As the valves move, they are able to store certain amount of mechanical energy transferred to them from the fluid in terms of kinetic energy and potential energy in the torsional springs. Part of the stored energy can be released back to

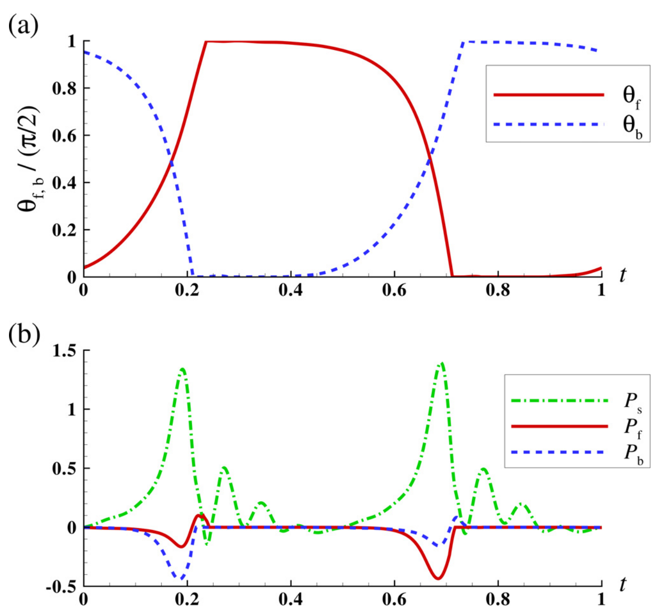

FIG. 3. (a) Rotations of the front valve (θ_f) and the back valve (θ_b), and (b) power expenditure of the shell (P_s), the front valve (P_f), and the back valve (P_b) during one cycle in steady state. $k_\theta = 10^{-4}$. $I_\theta = 10^{-4}$.

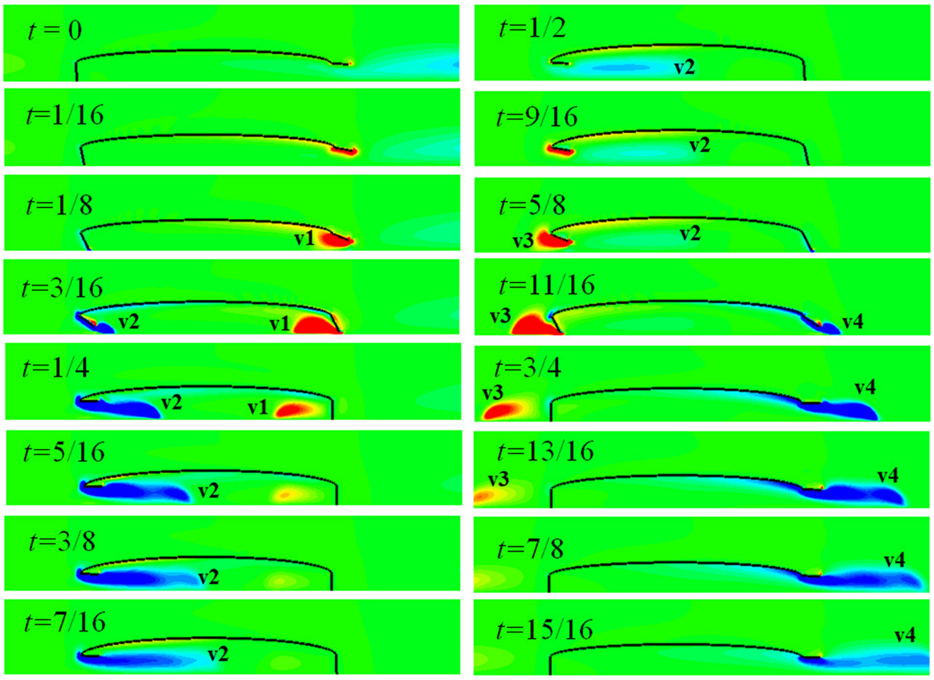

FIG. 4. Flow field around the body visualized through vorticity contour over one cycle in steady state. The vorticity range is from −40 (blue) to 40 (red). Concentration of positive vorticity corresponds to clockwise vortex, and negative vorticity corresponds to counterclockwise vortex. $k_\theta = 10^{-4}$, $l_\theta = 10^{-4}$.

the flow field, explaining the occasional occurrence of positive P_f and P_b. The oscillations in P_s are related to vorticity activities in the field, i.e., the generation, shedding, and evolution of vortices from the valves (see Fig. 4).

Figures 4 and 5 display the near-body flow fields, including the flow inside the pressure chamber, visualized through vorticity contours and streamlines, respectively. As the shell inflates and sucks fluid in (see $t = 0$ to $t = 1/2$ in the figures), two counter-rotating vortex rings

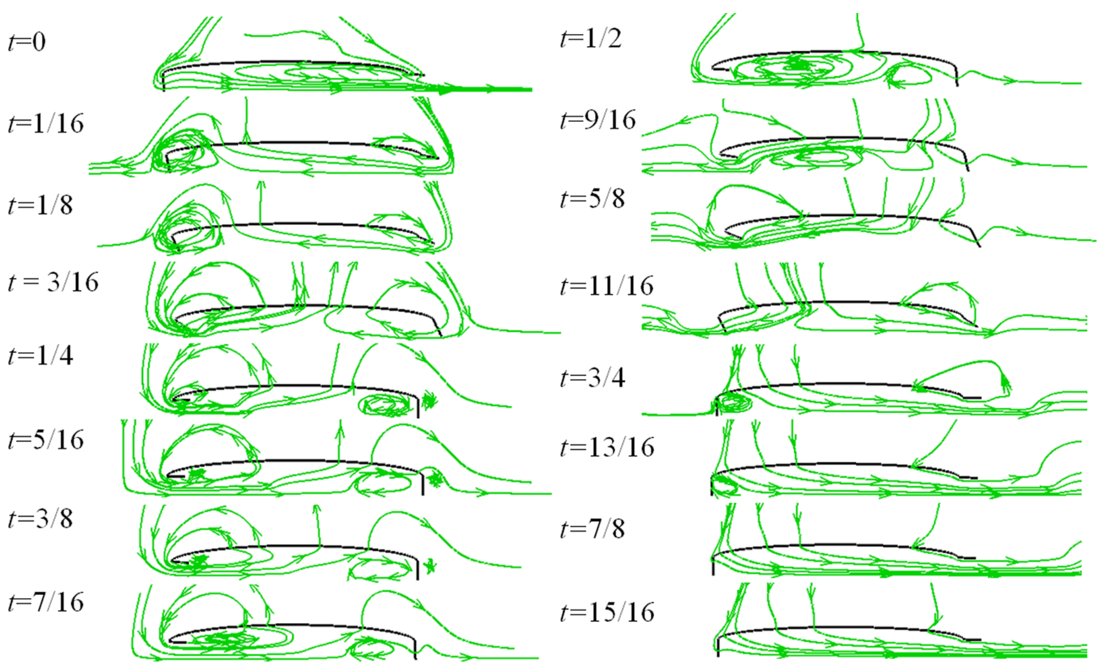

FIG. 5. Flow field around the body visualized through streamlines in a body-fixed reference system over one cycle in the steady state. $k_\theta = 10^{-4}$, $l_\theta = 10^{-4}$.

form. One (tagged as "v1" in the figure) is generated from the back valve, and the other one ("v2") from the front valve. They are formed when the inflowing fluid goes around the front and back valves, as shown by the streamlines. During deflation, the outgoing fluid also creates two vortices, v3 and v4, as it goes around the valves.

We then investigate the impact of valve design, hereby represented by the stiffness k_θ and the inertia I_θ, upon the dynamics and performance of the system. For this purpose, we first fix the value of I_θ at 10^{-4} and examine the cases when $k_\theta = 10^{-4}$, 10^{-3}, and 10^{-2}. When k_θ is below 10^{-4}, the results are relatively insensitive to its variation. The system works without the torsional spring, *per se*.

In Fig. 6, we plot time histories of the rotations of the two valves in the steady state in these three cases. As k_θ increases, there is a growing tendency for the valves to remain or go back to their closed configuration. Consequently, during deflation, when k_θ is large (e.g., $k_\theta = 10^{-2}$), the front valve goes back to the closed location quicker and remains there longer to prevent leaking through the front orifice [Fig. 6(a)]. Meanwhile, the fluid forcing is not able to keep the back valve fully open so that it is partially open most of the time [Fig. 6(b)]. This effectively reduces the diameter of the nozzle. It results in stronger jet and wake, as demonstrated in Fig. 7. For this reason, it is discovered that with I_θ fixed, the increase in k_θ leads to the generation of larger net force $\bar{F}_n$ (see Table I).

In our passive design, the activation of the front and back valves are achieved through their hydrodynamic interactions with the shell. Therefore, in stiffer valve cases, it takes more effort P_s to activate the shell [Fig. 8(a)]. The power transferred from the flow field to the valves to open them also significantly increases with stiffer valves, as we need to overcome the resistance from the spring [Figs. 8(b) and 8(c)]. However, there is no significant difference among the cases in terms of the magnitude of power transferred from the flow field to the valves as they are closing since there is no resistance from the springs in this

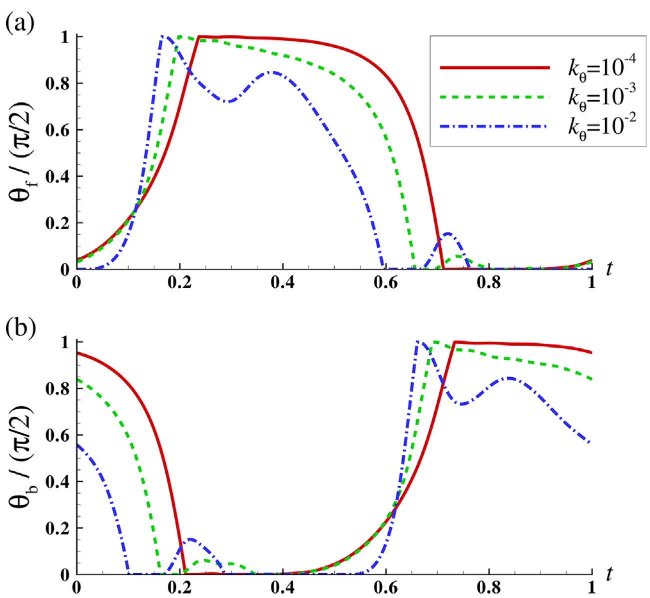

FIG. 6. Rotations of (a) the front valve and (b) the back valves during one cycle in the steady state at different values of k_θ. $I_\theta = 10^{-4}$.

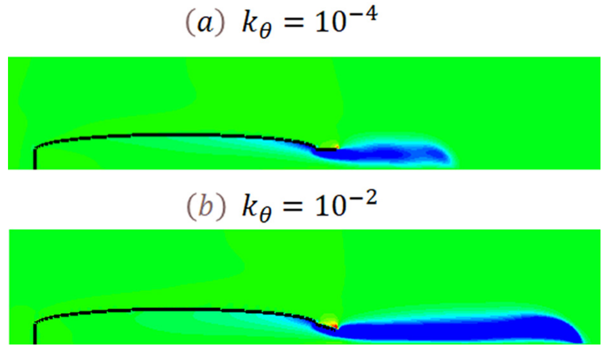

FIG. 7. Flow fields around the body visualized through vorticity contour at (a) $k_\theta = 10^{-4}$ and (b) $k_\theta = 10^{-2}$ at $t = 7/8$ during deflation. The vorticity range is from −40 (blue) to 40 (red). $I_\theta = 10^{-4}$.

process. In fact, the valve closure process is assisted by the release of the potential energy stored in the springs. That is why stiffer valves closes earlier than softer ones. Overall, the time-averaged power expenditure $\bar{P}_s$ increases with the increasing k_θ, as shown in Table I.

The dependencies of $\bar{F}_n$ and $\bar{P}$ upon k_θ remain unchanged in other values of I_θ.

We then study the effect of I_θ when k_θ is fixed. Figures 9 and 10 display the time histories of valve rotations and power expenditures within one cycle when steady state is established at three values of I_θ. The value of k_θ is fixed at 10^{-4}. It is seen that heavier valves move slower (Fig. 9) and consume more energy to move (Fig. 10). Although during deflation slower opening of the back valve effectively decreases the size of the nozzle and increases the jet speed, this beneficial effect on thrust generation is offset by opposite effects such as the leaking at the front valve during deflation. The net effect is that as I_θ increases the net force $\bar{F}_n$ decreases and the power expenditure $\bar{P}_s$ increases.

However, additional simulations show that the relative magnitudes of the beneficial and detrimental effects of increased inertia upon thrust generation may change when the spring stiffness is changed. For example, in Table III, we show the values of $\bar{F}_n$ when $k_\theta = 10^{-2}$ and $I_\theta = 10^{-5}$, 10^{-4}, and 3×10^{-4}. In this case, $\bar{F}_n$ rises with the increase in I_θ, which contradicts the trend shown in Table II when $k_\theta = 10^{-4}$. The dependence of $\bar{P}$ upon I_θ, on the other hand, remains unchanged.

The valve motions in the cases shown in Table III with a stiffer spring are displayed in Fig. 11. It is seen that similar to the cases with a softer spring (Fig. 9), the increase in valve inertia I_θ slows down the rotations of the valves, although the effect is less pronounced since the spring action now plays a more important role. One notable phenomenon is that at this case, the valves are not able to remain in the fully opened position for long. In the case, when $I_\theta = 10^{-5}$, the valves are

TABLE I. Time-averaged force generation and power expenditure of the system in the steady state in its tethered mode at different values of k_θ. $I_\theta = 10^{-4}$.

k_θ	$\bar{F}_n$	$\overline{P_s}$
10^{-4}	1.53×10^{-2}	0.225
10^{-3}	2.84×10^{-2}	0.315
10^{-2}	6.24×10^{-2}	0.741

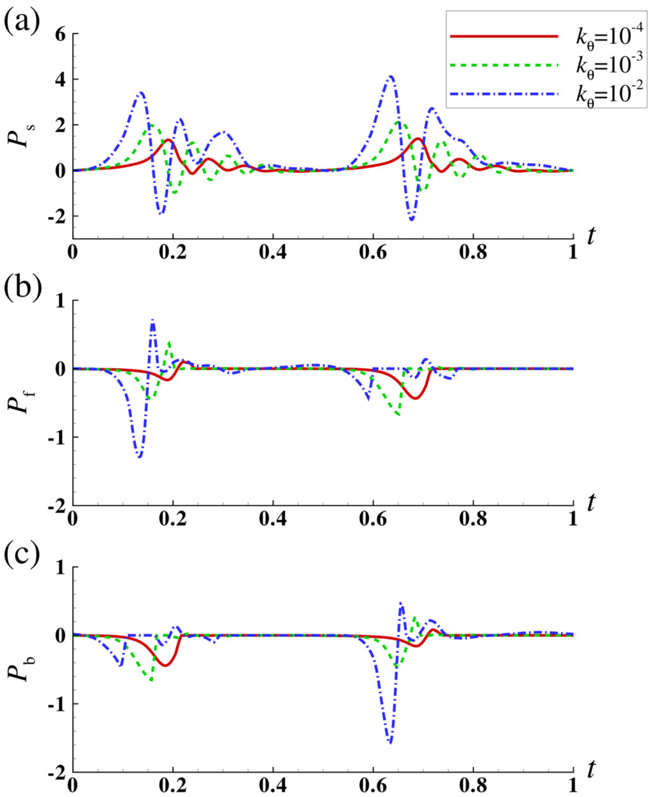

FIG. 8. Power expenditures of (a) the shell, (b) the front valve, and (c) the back valve during one cycle at different values of k_θ during one cycle in steady state. $I_\theta = 10^{-4}$.

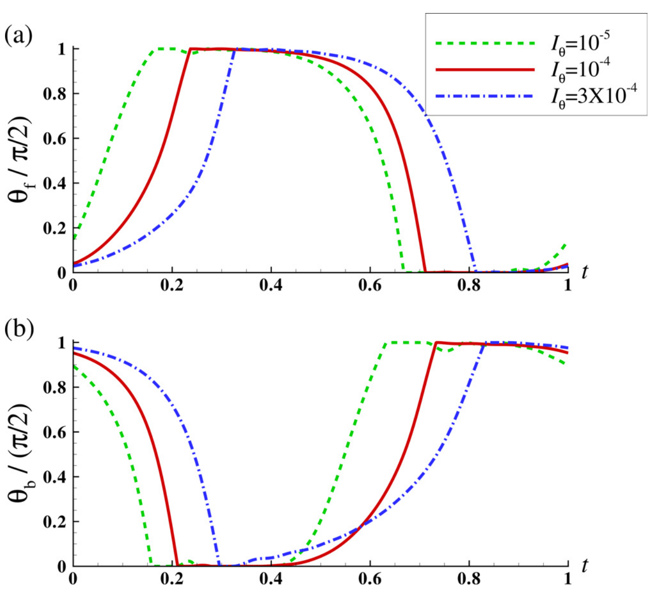

FIG. 9. Rotations of (a) the front valve and (b) the back valves during one cycle in the steady state at different values of I_θ. $k_\theta = 10^{-4}$.

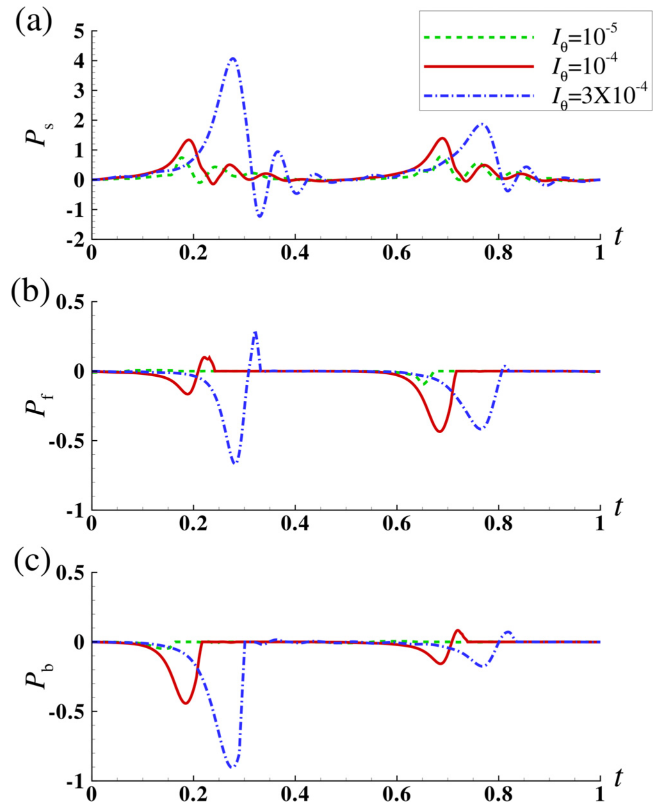

FIG. 10. Power expenditures of (a) the shell, (b) the front valve, and (c) the back valve during one cycle at different values of I_θ during one cycle in the steady state. $k_\theta = 10^{-4}$.

TABLE II. Time-averaged force generation and power expenditure of the system in the steady state in its tethered mode at different values of I_θ. $k_\theta = 10^{-4}$.

I_θ	$\bar{F}_n$	$\overline{P_s}$
10^{-5}	2.35×10^{-2}	0.128
10^{-4}	1.53×10^{-2}	0.225
3×10^{-4}	1.02×10^{-3}	0.474

TABLE III. Time-averaged force generation and power expenditure of the system in the steady state in its tethered mode at different values of I_θ. $k_\theta = 10^{-2}$.

I_θ	$\bar{F}_n$	$\overline{P_s}$
10^{-5}	5.67×10^{-2}	0.489
10^{-4}	6.24×10^{-2}	0.741
3×10^{-4}	7.11×10^{-2}	0.989

not able to reach the fully opened position at all, which may partially explain the (slightly) reduced thrust in this case.

The corresponding time histories of the power expenditures at $k_\theta = 10^{-2}$ and various valves of I_θ are shown in Fig. 12. They are qualitatively similar to the case with $k_\theta = 10^{-4}$ (see Fig. 10).

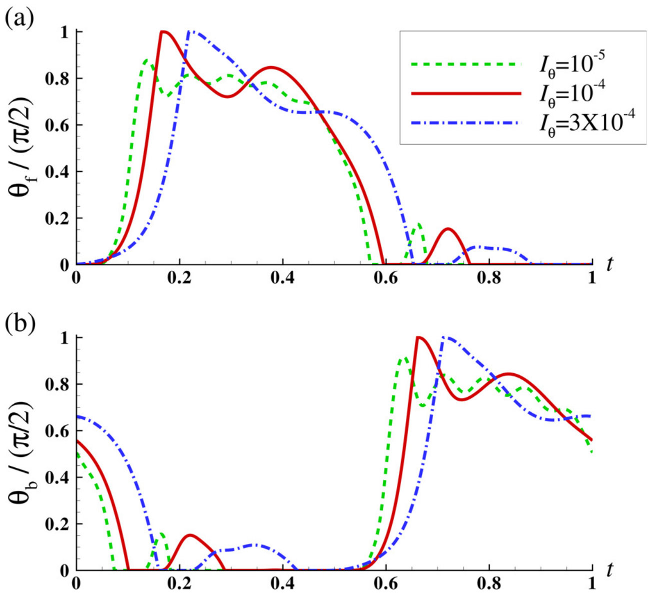

FIG. 11. Rotations of (a) the front valve and (b) the back valves during one cycle in the steady state at different values of I_θ. $k_\theta = 10^{-2}$.

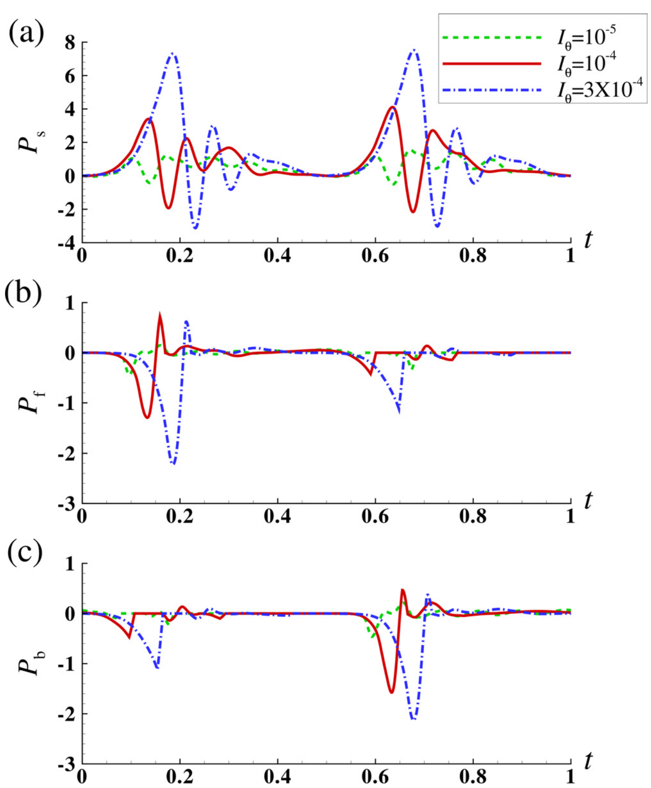

FIG. 12. Power expenditures of (a) the shell, (b) the front valve, and (c) the back valve during one cycle at different values of I_θ during one cycle in the steady state. $k_\theta = 10^{-2}$.

The net force generation and power expenditure of the system in its tethered mode over the range of k_θ from 10^{-6} to 10^{-2} and I_θ from 10^{-6} to 3×10^{-4} are summarized in Fig. 13. It is seen that large force generation is achieved when k_θ is high, especially if I_θ is also large (i.e., stiff and heavy valves). Unfortunately, this large force generation is accompanied by high power expenditure.

The study of the dynamics of the system in the tethered mode provides insights into its capacity of force generation. This mode roughly corresponds to the scenario when the system starts from rest. To evaluate the actual performance of the system with passive valves in locomotion, free-swimming tests are conducted in Subsection IV B.

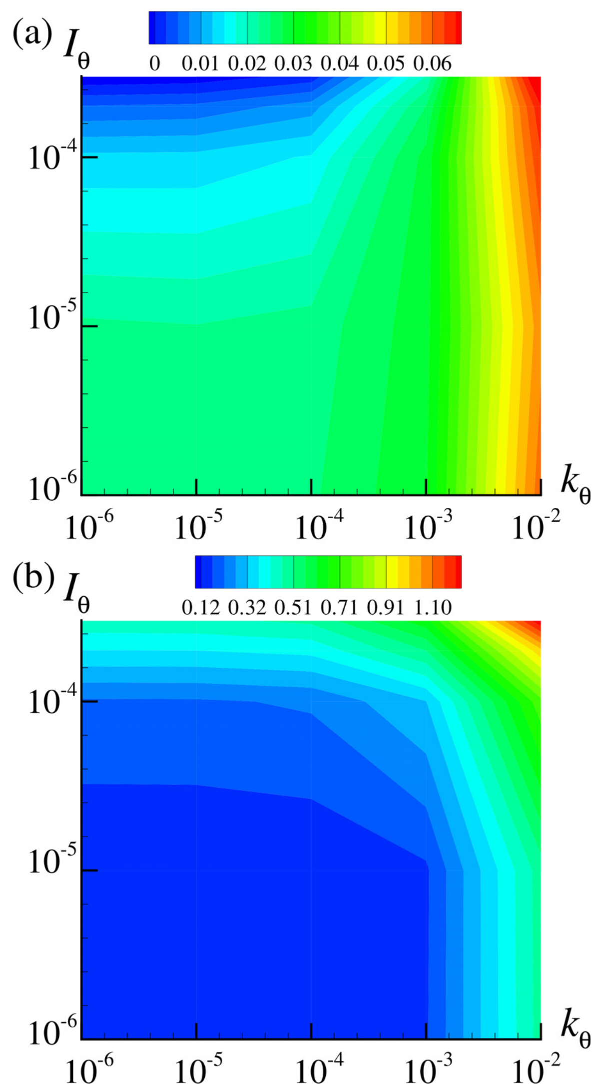

FIG. 13. Dependencies of (a) time-averaged net force $\bar{F}_n$ and (b) time-averaged power expenditure $\bar{P}_s$ upon stiffness k_θ and inertia I_θ of the valves in the tethered mode.

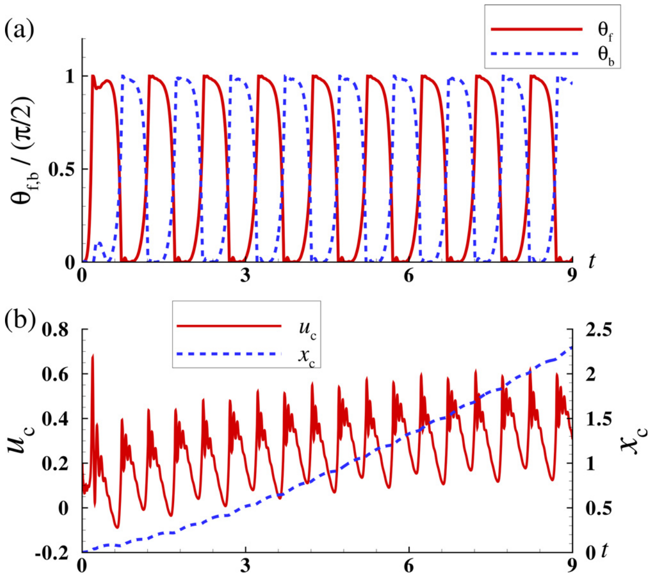

FIG. 14. Time histories of (a) rotations of the valves and (b) forward speed (u_c) and displacement (x_c) of the body in free swimming. $I_\theta = 10^{-4}$. $k_\theta = 10^{-4}$.

B. Free-swimming mode

In the free-swimming scenario, the forward motion of the body is calculated by using the Newton's law. To prevent the body from moving out of the computational domain, a uniform incoming flow with speed u_0 is introduced. The exact value of u_0 is case dependent and determined through numerical tests. During post processing, the effect of u_0 is removed through a transformation of reference systems so that all the results presented here are obtained in a fixed reference system without the background flow.

In the free-swimming mode, the performance is characterized by the following quantities: the time-averaged swimming speed $\bar{u}_c$, the time-averaged power expenditure $\bar{P}_s$, and the cost of transport $\mathrm{CoT} \equiv E/l$, where the energy expenditure E is obtained by integrating the power expenditure P_s over one period and l is the traveled distance during that period.

Figure 14 shows the motions of the two valves, the forward speed of the body and the forward displacement of the body in the free-swimming mode for a typical case with $I_\theta = 10^{-4}$ and $k_\theta = 10^{-4}$. It is seen that the opening and closing sequences of the valves are similar to those in the tethered case. Meanwhile, positive forward speed and forward displacement are achieved. After the steady state is reached, the time-averaged forward speed $\bar{u}_c$ in this particular case is 0.332 and the cost of transport CoT is 0.94.

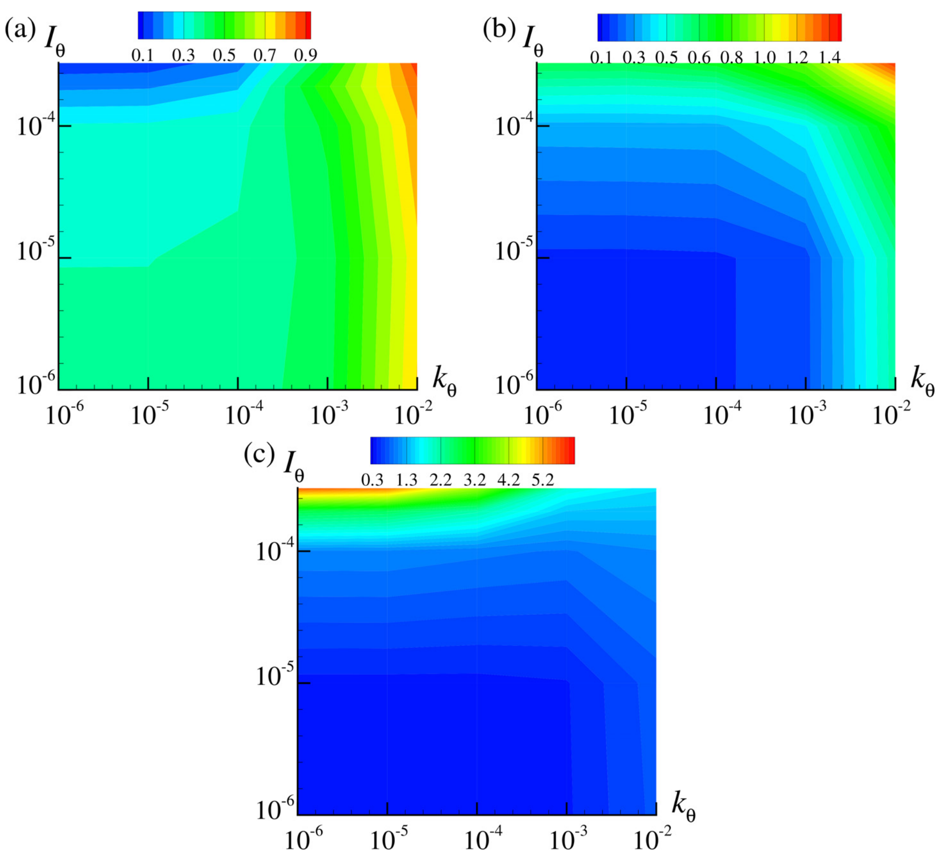

FIG. 15. Dependencies of (a) the time-averaged forward speed $\bar{u}_c$, (b) time-averaged power expenditure $\bar{P}_s$, and (c) CoT upon stiffness k_θ and inertia I_θ of the valves in the free-swimming mode.

Finally, in Fig. 15, we plot the dependencies of $\bar{u}_c$, $\bar{P}_s$, and CoT upon stiffness k_θ and inertia I_θ of the valves in the free-swimming mode. It is clear that the behaviors of $\bar{u}_c$ and $\bar{P}_s$ are similar to those of $\bar{F}_n$ and $\bar{P}_s$ in the tethered mode. Specifically, as shown in Fig. 15(a), large forward speed is reached when both k_θ and I_θ are large (i.e., stiff and heavy valves). However, in the parametric space that is also the location with large power expenditure [Fig. 15(b)] so that the corresponding CoT is not necessarily low.

Indeed, a better measure of the locomotion performance is the cost of transport, displayed in Fig. 15(c). Over the whole parametric space, we consider, the lowest CoT is 0.37, occurring when I_θ and k_θ are both at their minimum values, i.e., $I_\theta = 10^{-6}$ and $k_\theta = 10^{-6}$. However, at this point, the forward speed is also low ($\bar{u}_c = 0.12$). It turns out that CoT is relatively insensitive to variations in k_θ. For example, if we keep I_θ fixed at 10^{-6} while raising k_θ from 10^{-6} to 10^{-2}, the value of CoT increases from 0.37 to 0.47. On the other hand, if we keep k_θ fixed at 10^{-6} and increase I_θ from 10^{-6} to 3×10^{-4}, the value of CoT rises dramatically from 0.37 to 5.55. In fact, in terms of CoT, a soft and heavy valve delivers the worst performance. To guarantee decent efficiency, a safe choice is to use a light valve.

V. CONCLUSIONS

Using an immersed-boundary algorithm, we numerically investigated the locomotion performance of a swimmer inspired by the jet-propulsion mechanism of sea salps. We concentrated on one important question in the design of such a system: is it possible to use passive rather than actively controlled valves to accomplish the flow control procedure responsible for highly effective thrust generation?

Toward this end, we have created a simple model of the valves including their stiffness and inertia. Our simulations show that with this simple design, it is feasible to create the desired opening and closing motions of the valves which are synchronized with the expansion and shrinking deformations of the body. These synchronized motions and deformations not only generate positive thrust in the tethered mode, but also propel the body forward in the free-swimming scenario.

Systematic simulations have been conducted to illustrate effects of the design properties of the valves, hereby the rotational inertia and spring stiffness, upon the force generation capacity, and efficiency. The results show that if the inertia is fixed, increasing the spring stiffness will enhance the thrust generation and forward speed but decrease the efficiency, manifested in the increase in CoT. In the regime of relatively soft torsional springs when the inertia is increased, the thrust, the forward speed, and the efficiency all decrease. On the other hand, when the spring is sufficiently stiff, heavier valves may lead to increased thrust and speed, but decreased efficiency.

In comparison with actively controlled valves (referring to the systems in which external energy input is needed to directly control the motions of the valves), passive valves are mechanically simple since no controlling and actuation system is needed. In real devices, these valves may be built with flexible materials to further simplify the design. They may also be more adaptive in various swimming conditions where non-optimized motions of actively controlled valves could generate large drag force and compromise the performance. However, by removing external energy input, actively controlled valves should be able to duplicate any motions passive ones can do. Moreover, when external energy input is involved, they are also able to perform motions passive ones cannot do. For that reason, actively controlled valves work in a bigger parametric space in comparison with passive ones so that, in principle, they should perform better, although this performance enhancement is achieved at the cost of more complicated mechanical design.

AUTHOR DECLARATIONS

Conflict of Interest

The authors have no conflicts to disclose.

Author Contributions

Xiaobo Bi: Conceptualization (equal); Data curation (equal); Formal analysis (equal); Investigation (lead); Methodology (lead); Software (lead); Validation (lead); Writing – review & editing (equal). **Hui Tang:** Conceptualization (supporting); Investigation (supporting); Supervision (equal); Writing – review & editing (equal). **Qiang Zhu:** Conceptualization (lead); Data curation (lead); Formal analysis (equal); Investigation (equal); Methodology (equal); Project administration (lead); Resources (equal); Software (equal); Supervision (lead); Validation (equal); Visualization (lead); Writing – original draft (lead); Writing – review & editing (equal).

DATA AVAILABILITY

The data that support the findings of this study are available from the corresponding author upon reasonable request.

REFERENCES

[1] F. Giorgio-Serchi, A. Lidtke, and C. Laschi, "Biomimetic vortex propulsion: Toward the new paradigm of soft unmanned underwater vehicles," IEEE/ASME Trans. Mechatron. **18**, 484–493 (2013).
[2] F. Giorgio-Serchi, A. Arienti, and C. Laschi, "Underwater soft-bodied pulsed-jet thrusters: Actuator modeling and performance profiling," Int. J. Rob. Res. **35**, 1308–1329 (2016).
[3] C. Christianson, Y. Cui, M. Ishida, X. Bi, Q. Zhu, G. Pawlak, and M. Tolley, "Cephalopod-inspired robot capable of cyclic jet propulsion through shape change," Bioinspiration Biomimetics **16**, 016014 (2020).
[4] T. Bujard, F. Giorgio-Serchi, and G. Weymouth, "A resonant squid-inspired robot unlocks biological propulsive efficiency," Sci. Rob. **6**, eabd2971 (2021).
[5] J. Gosline and M. DeMont, "Jet-propelled swimming in squid," Sci. Am. **252**, 96–103 (1985).
[6] H. Neumeister, B. Ripley, T. Preussm, and W. W. F. Gilly, "Effects of temperature on escape jetting in the squid," J. Exp. Biol. **203**, 547–557 (2000).
[7] Q. Zhu and Q. Xiao, "Physics and applications of squid-inspired jetting," Bioinspiration Biomimetics **17**, 041001 (2022).
[8] X. Bi and Q. Zhu, "Fluid-structure interaction of a squid-inspired swimmer," Phys. Fluids **31**, 101901 (2019).
[9] X. Bi and Q. Zhu, "Pulsed-jet propulsion via shape deformation of an axisymmetric swimmer," Phys. Fluids **32**, 018902 (2020).
[10] Y. Luo, Q. Xiao, Q. Zhu, and G. Pan, "Pulsed-jet propulsion of a squid-inspired swimmer at high Reynolds number," Phys. Fluids **32**, 111901 (2020).
[11] Y. Luo, Q. Xiao, Q. Zhu, and G. Pan, "Jet propulsion of a squid-inspired swimmer in the presence of background flow," Phys. Fluids **33**, 031909 (2021).
[12] A. Hoover, A. Porras, and L. Miller, "Pump or coast: The role of resonance and passive energy recapture in medusan swimming performance," J. Fluid Mech. **863**, 1031–1061 (2019).
[13] S. Spagnolie and M. Shelley, "Shape changing bodies in squid: Hovering, ratcheting, and bursting," Phys. Fluids **21**, 013103 (2009).
[14] S. Steele, G. Weymouth, and M. Triantafyllou, "Added mass energy recovery of octopus-inspired shape change," J. Fluid Mech. **810**, 155–174 (2017).
[15] P. Linden and J. Turner, "The formation of 'optimal' vortex rings, and the efficiency of propulsion devices," J. Fluid Mech. **427**, 61–72 (2001).

[16]X. Bi and Q. Zhu, "Numerical investigation of cephalopod-inspired locomotion with intermittent bursts," Bioinspiration Biomimetics **13**, 056005 (2018).
[17]I. Bartol, P. Krueger, W. Stewart, and J. Thompson, "Hydrodynamics of pulsed jetting in juvenile and adult brief squid *Lolliguncula brevis*: Evidence of multiple jet 'modes' and their implications for propulsive efficiency," J. Exp. Biol. **212**, 1889–1903 (2009).
[18]X. Bi and Q. Zhu, "Efficiency of pulsed-jet propulsion via thrust-drag decomposition," Phys. Fluids **33**, 071902 (2021).
[19]X. Bi and Q. Zhu, "Role of internal flow in squid-inspired jet propulsion," Phys. Fluids **34**, 031906 (2022).
[20]Q. Bone and E. Trueman, "Jet propulsion in salps (Tunicata: Thaliacea)," J. Zool. **201**, 481–506 (1983).
[21]L. Madin, "Aspects of jet propulsion in salps," Can. J. Zool. **68**, 765–777 (1990).
[22]X. Bi, H. Tang, and Q. Zhu, "Valve-mediated flow control in salp-like locomotion," Phys. Fluids **34**, 051913 (2022).
[23]K. Sutherland and L. Madin, "Comparative jet wake structure and swimming performance of salps," J. Exp. Biol. **213**, 2967–2975 (2010).
[24]M. Gharib, R. Rambod, and K. Shariff, "A universal time scale for vortex ring formation," J. Fluid Mech. **360**, 121–140 (1998).
[25]K. Sutherland and D. Weihs, "Hydrodynamic advantages of swimming by salp chains," J. R. Soc. Interface **14**, 20170289 (2017).
[26]H. Jiang, J. Costello, and S. Colin, "Fluid dynamics and efficiency of colonial swimming via multijet propulsion at intermediate Reynolds numbers," Phys. Rev. Fluids **6**, 013103 (2021).
[27]E. Munoza and S. L. Clainche, "On the topology patterns and symmetry breaking in two planar synthetic jets," Phys. Fluids **34**, 024103 (2022).
[28]X. Bi and Q. Zhu, "Free swimming of a squid-inspired axisymmetric system through jet propulsion," Bioinspiration Biomimetics **16**, 066023 (2021).
[29]R. Beam and R. Warming, "An implicit factored scheme for the compressible Navier-Stokes equations," AIAA J. **16**, 393–402 (1978).
[30]D. Goldstein, R. Handler, and L. Sirovich, "Modelling a no-slip flow boundary with an external force field," J. Comput. Phys. **105**, 354–366 (1993).
[31]P. Linden and J. Turner, "Optimal vortex rings and aquatic propulsion mechanisms," Proc. R. Soc. London, Ser. B **271**, 647–653 (2004).
[32]J. Dabiri, "Optimal vortex formation as a unifying principle in biological propulsion," Annu. Rev. Fluid Mech. **41**, 17–33 (2009).